



**HAL**  
open science

## Hydraulic conductivity and microstructure changes of compacted bentonite/sand mixture during hydration

Qiong Wang, Yu-Jun Cui, Anh Minh A.M. Tang, Jean-Dominique Barnichon, Simona Saba, Wei-Min Ye

► **To cite this version:**

Qiong Wang, Yu-Jun Cui, Anh Minh A.M. Tang, Jean-Dominique Barnichon, Simona Saba, et al.. Hydraulic conductivity and microstructure changes of compacted bentonite/sand mixture during hydration. *Engineering Geology*, 2013, 164, pp.67-76. 10.1016/j.enggeo.2013.06.013 . hal-00926873

**HAL Id: hal-00926873**

**<https://enpc.hal.science/hal-00926873>**

Submitted on 25 Apr 2018

**HAL** is a multi-disciplinary open access archive for the deposit and dissemination of scientific research documents, whether they are published or not. The documents may come from teaching and research institutions in France or abroad, or from public or private research centers.

L'archive ouverte pluridisciplinaire **HAL**, est destinée au dépôt et à la diffusion de documents scientifiques de niveau recherche, publiés ou non, émanant des établissements d'enseignement et de recherche français ou étrangers, des laboratoires publics ou privés.



30 **Abstract:**

31 Compacted bentonite-based materials are often considered as sealing/backfill  
32 materials in deep geological repository for high level radioactive waste. A good  
33 understanding of their hydration process is essential as this process is directly related  
34 to over-pack corrosion and nuclide migration. In this study, the unsaturated hydraulic  
35 properties of MX80 bentonite/sand mixture were characterized by carrying out a  
36 series of experiments including water retention test, infiltration test as well as  
37 microstructure observation. It was found that with suction decrease under constant  
38 volume condition, the hydraulic conductivity decreased followed by an increase after  
39 a suction threshold. At suctions higher than 12.6 MPa, hydration led to progressive  
40 large-pores clogging by exfoliation of clay particles. On the contrary, when saturation  
41 was approached (suction lower than 4.2 MPa), the large-pores quantity increased due  
42 to the creation of two-dimensional pores. It was also observed that the soil hydraulic  
43 conductivity changed following the same tendency as the large-pores quantity during  
44 hydration. In other words, water transfer was primarily governed by the network of  
45 large-pores.

46

47 **Keywords:** bentonite/sand mixture; suction; constant-volume condition; hydraulic  
48 conductivity; microstructure

49

## 50 1 INTRODUCTION

51 Most concepts of deep geological repository for high level radioactive waste are based  
52 on the multi-barrier system consisting of the natural barrier (host rock) and engineered  
53 barriers (waste container, buffer and sealing elements). One of the most important  
54 functions of the engineered barrier is to create a zone of low permeability for  
55 separating the high-level radioactive waste from the surrounding environment  
56 (Komine, 2010). Bentonite-based materials are often chosen as sealing/backfill  
57 materials in this multi-barrier system due to their low permeability, high swelling and  
58 high radionuclide retardation capacities (Pusch, 1979; Yong et al., 1986; Villar et al.,  
59 2008).

60 Once emplaced in the repository, the bentonite-based materials start to be hydrated by  
61 the pore water infiltrating from the host-rock. These materials absorb water and swell.  
62 Firstly, the technological voids are filled up, with a decrease in dry density. Then, the  
63 subsequent swelling is restrained by the host rock and swelling pressure develops  
64 under constant volume conditions. The hydration under this constant volume  
65 condition corresponds to a coupled hydro-mechanical process with involvement of  
66 microstructure changes. A proper understanding of this process is essential for well  
67 controlling the water transfer-related phenomena as over-pack corrosion, nuclide  
68 migration, etc.

69 A number of studies have been performed to study the water transfer in  
70 bentonite-based materials in both saturated state (Kenney et al., 1992; Dixon et al.,

71 1999; Komine, 2004, etc) and unsaturated state (Börgesson, 2001; Loiseau et al., 2002;  
72 Kröhn, 2003a, 2003b; Lemaire et al., 2004; Cui et al., 2008). The saturated hydraulic  
73 conductivity has been found to be strongly dependent on the initial dry density (Dixon,  
74 1999; Karnland et al., 2008, etc.). Under unsaturated conditions with  
75 suction-dependent water flow, the hydraulic conductivity was often determined using  
76 the instantaneous profile method (Daniel, 1982). Following this method, Cui et al.  
77 (2008) investigated the unsaturated hydraulic conductivity of the Kunigel  
78 bentonite/sand mixture and observed that with suction decrease under constant  
79 volume conditions, the hydraulic conductivity decreases followed by an increase after  
80 certain suction threshold. Ye et al. (2009) obtained similar results on GMZ bentonite.  
81 Thomas et al. (2003) and Villar et al. (2005) also pointed out that, in expansive  
82 materials, hydraulic conductivity decreases with the increase in degree of saturation,  
83 due to microstructural modifications. This is different from the common results  
84 showing that the hydraulic conductivity of unsaturated soils increases with suction  
85 decrease (van Genuchten, 1980; Fredlund and Rahardjo, 1993). The particular trend  
86 observed for bentonite-based materials adds a degree of complexity when dealing  
87 with the long term behaviour of these materials. Without considering this  
88 phenomenon, the water transfer in bentonite-based materials will be over-estimated.  
89 Thus, it is of great importance to go in depth of this phenomenon by considering the  
90 coupled hydro-mechanic changes during the hydration process.

91 If the phenomenon of the particular hydraulic conductivity changes with suction  
92 decrease for bentonite-based materials was evidenced experimentally (Cui et al., 2008;

93 Ye et al.; 2009), the explanation has been not yet confirmed by microstructure  
94 analysis. The present study aims at completing this lack by investigating the hydraulic  
95 properties of a compacted bentonite-sand mixture and the microstructure changes  
96 during the hydration process. Infiltration test and water retention test were first carried  
97 out under constant volume conditions allowing the determination of hydraulic  
98 conductivity by the instantaneous profile method. The study was then completed with  
99 the microstructure observation allowing analysing the effect of microstructure change  
100 on the variations of hydraulic conductivity. All tests were carried out at constant  
101 ambient temperature ( $20\pm 1^\circ\text{C}$ ), and the effect of temperature was not considered in  
102 this study.

## 103 **2 MATERIALS AND METHODS**

### 104 **2.1 Materials and samples preparation**

105 The soil studied is a mixture of MX80 bentonite and quartz sand with a proportion of  
106 70/30 in dry mass. The bentonite is from Wyoming, USA, with a high content of  
107 montmorillonite (80%). It has a liquid limit of 575%, a plastic limit of 53% and a unit  
108 mass of  $2.77 \text{ Mg/m}^3$ . The cation exchange capacity (CEC) is 76 meq/100g (83 % of  
109  $\text{Na}^+$ ). The grain size distribution (Figure 1) determined by hydrometer (French  
110 standard AFNOR NF P94-057) on deflocculated clay shows that the fraction of  
111 clay-size particles ( $< 2 \mu\text{m}$ ) is 84%.

112 The sand used in the mixture was from Eure and Loire (France), with a unit mass of  
113 sand grains of  $2.65 \text{ Mg/m}^3$ . It was sieved at 2 mm prior to being mixed with the

114 bentonite. Figure 1 shows the grains size distribution curve determined by the dry  
115 sieving method (AFNOR NF P94-056). The curve for sand is characterized by a  
116 uniformity coefficient  $C_u$  of 1.60 and a  $D_{50}$  close to 0.6 mm. This curve is close to that  
117 of bentonite powder obtained by “dry” sieving (see in Figure 1).

118 Synthetic water having similar chemical composition to that of the pore water of the  
119 Callovo-Oxfordian claystone (TDS = 5.7 g/L) from the ANDRA Underground  
120 Research Laboratory (URL) in Bure (France) was used for the infiltration test (Table  
121 1). For the preparation of the synthetic water, the chemical components in powder  
122 were mixed with distilled water using a magnetic stirrer until full dissolution.

123 For the samples preparation, the bentonite powder has a hygroscopic water content of  
124 12.2% was carefully mixed with dry sand (70% bentonite - 30% sand in mass) giving  
125 a mixture at a water content of 8.5%. The mixture powder was then put into a  
126 hermetic container connected to a vapor circulation system containing free water  
127 (100% relative humidity), so as to reach a target water content of 11.0%. The grain  
128 size distribution curve of the mixture powder is presented in Figure 1. It shows a well  
129 graded distribution around a mean diameter of 0.9 mm.

130 The soil specimens for both the infiltration and water retention tests were obtained by  
131 compaction of the bentonite/sand mixture powder at its water content of 11.0%. A  
132 given quantity of the mixture was placed in a metallic mould and statically compacted  
133 to a dry density of  $1.67 \text{ Mg/m}^3$ . The initial suction of the compacted samples was  
134 about 65 MPa (measured using a relative humidity sensor after compaction). For the  
135 infiltration test, the specimen (250-mm long and 50 mm in diameter) was compacted

136 in 5 layers of 50-mm thickness each.

## 137 **2.2 Experimental method**

138 The hydraulic conductivity of the unsaturated bentonite/sand mixture was determined  
139 using the instantaneous profile method, which requires both suction and volumetric  
140 water content profiles (Daniel, 1982; Cui et al., 2008; Ye et al., 2009). The suction  
141 profile (corresponding to the total suction) was obtained by monitoring the relative  
142 humidity (RH) changes in an infiltration test, whereas the volumetric water content  
143 profile was deduced from the water retention curve determined separately.

### 144 **2.2.1 Infiltration test**

145 The hydration cell used for the infiltration test is presented in Figure 2. After  
146 compaction, the soil specimen (50 mm in diameter and 250-mm long) was carefully  
147 introduced into the cylindrical cell (50 mm in inner diameter) with the ends of the two  
148 cells jointed together. The hydration cell is made of stainless steel, which hindered  
149 any lateral volume changes. Four relative humidity (RH) sensors were installed every  
150 50 mm along the sample ( $h = 50, 100, 150, 200$  mm from the wetting end) through the  
151 ports in the wall of the cell. The RH sensor consists of a unique capacitive sensor  
152 element for RH measurement and a stainless steel shell (12 mm in external diameter)  
153 for protecting the sensors from deformation and corrosions. Two ends of the cell were  
154 tightly closed by metallic discs of 40 mm thickness each. Water supply was done at  
155 the atmospheric pressure through the water inlets in the bottom base, which was  
156 connected to burettes. The top cover has an outlet for air expulsion. To avoid water



157 evaporation, a deflated balloon-shaped membrane was used to cover the air outlet.  
158 The air in the membrane was released regularly in order to keep an air pressure close  
159 to the atmospheric one. The water volume injected into the sample was also measured  
160 during the test by monitoring the water level in the burettes.

161 At the end of the infiltration test, the sample was extruded by pushing the top side,  
162 about 12 MPa pressure was applied for this purpose. Several small specimens at  
163 different positions along the column were taken for the water content and dry density  
164 determinations. The water content of the sample was measured by oven drying, while  
165 the dry density was determined based on the fluid displacement technique (see Head,  
166 1980, Geiser, 1999) using an immiscible oil Kerdane (with a density of 0.791 at  
167 20°C).

### 168 **2.2.2 Water retention curve**

169 The water retention curve of the bentonite/sand mixture under constant volume  
170 condition was determined by controlling the suction using both the vapour  
171 equilibrium technique (for suctions higher than 4.2 MPa) and osmotic technique (for  
172 suctions of 1 and 0.1 MPa). It is worth noting that the vapour equilibrium technique  
173 controls total suction whereas the osmotic technique controls matric suction (see  
174 Delage 1998a; Delage and Cui, 2008; Blatz et al.; 2008 for more detailed). The zero  
175 suction was imposed by injecting the synthetic water (Table 1) into the sample.

176 The compacted sample (50 mm in diameter and 5 mm in height) was placed in a  
177 stainless steel cell. Two porous disks were put at both sides of the sample allowing

178 vapour or water flow. To apply the osmotic technique, a semi-permeable membrane  
179 was placed between the porous stone and the soil sample (Figure 3a), the whole was  
180 then sandwiched between two perforated discs and immersed in a PEG 20 000  
181 (Polyethylene Glycol) solution at a concentration corresponding to the required  
182 suction (see Table 2). Several drops of penicillin were added in the solution to prevent  
183 from attack of bacteria. To apply suction with the vapour equilibrium technique, the  
184 sample sandwiched between two porous stones was installed between two external  
185 plates with valves (Figure 3b) that were connected to a device containing a saturated  
186 salt solution for relative humidity control (see Wang et al., 2012 for more details).  
187 Following this technique, 2-4 weeks was required to reach the equilibrium (Marcial,  
188 2003; Tang & Cui, 2005). However, the equilibrium time was much shorter for the  
189 osmotic technique as it allows liquid water exchanges between the soil sample and the  
190 PEG solution (Blatz et al., 2008). In this study, the equilibration time was extended to  
191 2 months for both the vapour equilibrium technique and osmotic technique and the  
192 water content of all samples was determined by weighing at the end.

193 All water retention tests performed and the solutions used for suction control are  
194 presented in Table 2. As shrinkage may occur upon drying, it was not possible to  
195 control sample volumes along drying paths. Thus, only the wetting curve was  
196 determined under restrained-swell conditions. This was enough for the purpose of  
197 hydraulic conductivity determination based on the infiltration test under constant  
198 volume conditions.

### 199 **2.2.3 Microstructure observation**

200 Mercury Intrusion Porosity (MIP) and Scanning Electron Microscope (SEM) tests  
201 were carried out on freeze-dried samples, which had been equilibrated at different  
202 suctions under constant volume conditions. The suction values considered ranged  
203 from 65 MPa (as-compacted state) to zero (saturated state). For as-compacted samples,  
204 it was cut to small slices and freeze-dried (see Delage & Lefevbre, 1984; Cui et al.,  
205 2002., Delage et al., 2006; Tang et al., 2011 for more details). Samples for other  
206 suctions were taken from the water retention test under constant volume conditions  
207 (Table 2 for details). Each sample was cut to two parts, one for the preparation of  
208 samples for the microstructure observation and another for water content  
209 determination by weighing (for water retention curve).

## 210 **3 EXPERIMENTAL RESULTS**

211 Figure 4 depicts the water retention curve (suction versus the gravimetric water  
212 content) obtained along the wetting path under constant-volume conditions. In the  
213 plane of gravimetric water content versus suction (Figure 4), a bi-linear water  
214 retention curve was obtained: water content increases linearly with suction decrease  
215 when this latter is higher than 1 MPa; at lower suctions the water content remains  
216 constant and the water retention curve is almost horizontal. The inflexion of the WRC  
217 (1 MPa) can be considered as the air-entry value of the sample.

218 At the end of the infiltration test, the sample was removed by pushing it from the top.

219 The water content and dry density along the column were determined and shown in  
220 Figure 5. As expected, the water content decreased with increasing distance from the  
221 wetting end. Regarding the dry density distribution, a lower dry density than at the  
222 initial state (1.62-1.65 Mg/m<sup>3</sup> against 1.67 Mg/m<sup>3</sup>) was obtained in the near wetting  
223 end zone (h = 0-40 mm); a dry density close to the initial one (1.67-1.68 Mg/m<sup>3</sup>  
224 against 1.67 Mg/m<sup>3</sup>) was obtained in the middle zone (h = 50-150 mm); in the upper  
225 zone (h = 200 - 250 mm), a significant dry density increase up to 1.73 Mg/m<sup>3</sup> was  
226 identified.

227 During the infiltration test, RH changes over time were monitored and plotted in  
228 Figure 6 for all measurement positions (h = 50, 100, 150 and 200 mm). The initial RH  
229 was 62 ± 1% corresponding to a suction of 64.5 ± 1.5 MPa. Once the infiltration  
230 started, the value of the RH at h = 50 mm increased rapidly and reached 90% after  
231 500 h, then increased gradually to 98.30% after 1900 h. The value of the sensors at h  
232 = 100, 150 and 200 mm started to increase after about 200 h, 500 h and 1900 h  
233 respectively. The larger the distance from the wetting end the lower the increasing rate  
234 of RH.

235 The total suction (*s*) was then calculated from RH value using Kelvin's law:

$$236 \quad s = -(\rho_w RT / M_w) \ln(RH/100) \quad \text{Eq. (1)}$$

237 where  $\rho_w$  is the water unit mass (1 Mg/m<sup>3</sup>); *R* is the universal (molar) gas constant  
238 (8.31432 J/mol K); *T* is the absolute temperature (K), equal to (273.15+20) °C in this  
239 study; *M<sub>w</sub>* is the molecular mass of water vapour (18.016 kg/kmol).

240 Figure 7 depicts the suction isochrones for every 400 h. Note that the suction value at  
 241  $h = 250$  mm was not monitored and it was estimated by linearly extending the curves  
 242 between  $h = 150$  mm and  $h = 200$  mm. At  $t = 0$ , the initial suction of the sample was  
 243 quite homogeneous, with a mean value of  $64.5 \pm 1.5$  MPa. It was supposed that after  
 244 starting the infiltration, the suction at the wetting face  $h = 0$  mm decreased rapidly to  
 245 zero. The total suction at  $h = 50$  mm decreased to 2.37 MPa at  $t = 2200$  h while the  
 246 total suction at  $h = 200$  mm started to decrease at  $t = 1900$  h, and remained high ( $s =$   
 247 33.84 MPa) at  $t = 6000$  h.

248 Based on the suction profiles (Figure 7), the hydraulic gradients ( $i$ ) and water fluxes  
 249 ( $q$ ) at each measurement section ( $h$ ) and time ( $t$ ) were deduced following the methods  
 250 shown in Figure 8. The hydraulic gradients were calculated as the tangent of suction  
 251 profiles ( $s$  and  $h$  are expressed in m) as indicated in Figure 8a and the water fluxes  
 252 were determined by integrating the difference in the volumetric water content profiles  
 253 at a time interval ( $\Delta t$ ) as indicated in Figure 8b.

254 To calculate the water flux, the volumetric water content of the mixture was deduced  
 255 from the total suction using the water retention curve obtained at constant-volume  
 256 conditions (Figure 4). As the suction measured by RH sensors in the infiltration test  
 257 ranges from 2.37 MPa to 65 MPa, Eq. 2 (see also Figure 4) was used to calculate the  
 258 gravimetric water content from suction, and the volumetric water content ( $\theta$ ) can be  
 259 then calculated using Eq.3:

$$260 \quad w = -7.261 \text{Log}(s) + 24.102 \quad (\text{Eq. 2})$$

$$261 \quad \theta = w \rho_d / \rho_w \quad (\text{Eq. 3})$$

262 where,  $\rho_d$  is assumed to be constant ( $1.67 \text{ Mg/m}^3$ ) during infiltration under constant  
263 volume conditions.

264 In order to verify the validity of these calculations, the total volume of water passing  
265 through each section was calculated from the volumetric water content profiles. The  
266 sum of these volumes from  $h = 0 \text{ mm}$  to  $h = 250 \text{ mm}$  corresponds to the volume of  
267 water absorbed by the soil specimen during infiltration. Figure 9 shows the  
268 comparison between the injected volume of water and that estimated from the water  
269 content profiles. It can be observed that there is a good agreement between the  
270 measured and calculated values, confirming the validity of the analyses performed.

271 Using the suction profiles presented in Figure 7, the hydraulic gradient ( $i$ ) and water  
272 fluxes ( $q$ ) at the four measurement sections  $h = 50 \text{ mm}$ ,  $100 \text{ mm}$ ,  $150 \text{ mm}$  and  $200$   
273  $\text{mm}$  for each  $100 \text{ h}$  were obtained, and used to calculate the hydraulic conductivity by  
274 applying Darcy's law (Eq.4). The hydraulic conductivity determined is plotted versus  
275 suction in Figure 10. It can be seen that at different measurement sections different  
276 relationships were obtained.

277 
$$k_w = -\frac{1}{A} \cdot \frac{q}{\frac{1}{2}(i_t + i_{t+\Delta t})} \quad (\text{Eq. 4})$$

278 where,  $k_w$  is the hydraulic conductivity;  $i_t$  and  $i_{t+\Delta t}$  are the hydraulic gradients at  
279 instant  $t$  and  $t+\Delta t$ , respectively.

280 The pore size distribution curves for suctions ranging from  $65 \text{ MPa}$  (initial state) to  
281  $12.6 \text{ MPa}$  are presented in Figure 11a and Figure 11b. It was observed in Figure 11a

282 that the final values of the intruded mercury void ratio ( $e_{mi}$ ) were lower than the  
283 global soil void ratio ( $e = 0.63$ ). Moreover, the amount of non-intruded porosity ( $e_{mi} =$   
284  $0.47$  in the initial state) decreased with suction decrease. From the derivative curves  
285 (Figure 11b), a typical bimodal porosity was identified in the initial state ( $\rho_d = 1.67$   
286  $\text{Mg/m}^3$ ,  $s = 65$  MPa), and two pore groups can be defined: small-pores having a mean  
287 size of  $0.02 \mu\text{m}$  and large-pores having a mean size of  $50 \mu\text{m}$ . Following the  
288 classification detailed in Stepkowska (1990) and Villar et al. (2012), these two pore  
289 families correspond to the categories of mesopores ( $0.002\text{-}0.05 \mu\text{m}$ ) and macropores  
290 ( $> 0.05 \mu\text{m}$ ), respectively. The application of  $38$  MPa suction resulted in significant  
291 decrease of large-pores quantity (about  $10\%$ ), and little changes in small-pores  
292 (Figure 11b). However, no obvious further changes in both the large-pores and  
293 small-pores can be observed for the subsequent decrease of suction ( $38 - 24.8 - 12.6$   
294 MPa).

295 Figures 11c and 11d show the curve for  $4.2$ ,  $1$  and  $0$  MPa suction, lower values of  
296 non-intruded void ratio  $e_{mi}$  were also obtained compared to the global void ratio of the  
297 soil (Figure 11c). However, it was found that the intruded porosity at these suctions  
298 was slightly higher than that in the initial state ( $s = 65$  MPa,  $e_{mi} = 0.47$ ). From the  
299 derivative curves (Figure 11d), it was clearly seen that this increased intruded porosity  
300 corresponded to the difference in large-pores volume, as the small-pores volume  
301 decreased with decreasing suction. Moreover, a third pore family (with pore size of  
302  $0.1\text{-}2 \mu\text{m}$ ) appeared for the saturated sample.

303 The pore size distribution analyse was completed using the SEM technique (Figure  
304 12). The photos were taken at two scales which focused on the behaviour of mixture  
305 (1250 x 1000  $\mu\text{m}$ ) and bentonite aggregates (25 x 20  $\mu\text{m}$ ), respectively. The sand  
306 grains cannot be identified in the photos at lower magnification (picture size of 1250 x  
307 1000  $\mu\text{m}$ ). The photograph taken at the initial state ( $s = 65 \text{ MPa}$ ) clearly shows the  
308 large-pores with a maximum diameter of about 100  $\mu\text{m}$  (Figure 12a), which is in  
309 agreement with the MIP results from Figure 11a. Figure 12b shows that the  
310 aggregates were densely assembled. The small-pores observed in the MIP test (0.02  
311  $\mu\text{m}$ ) cannot be detected by the SEM technique. Comparison of the photographs of 38  
312 MPa suction (Figure 12d) and 65 MPa suction (Figure 12b) shows that the clay  
313 particles exfoliation occurred when suction decreased. The photographs at saturated  
314 state (Figure 12e and 12f) show that the large-pores observed at higher suctions  
315 (Figure 12a and 12c) were filled by the swollen bentonite; however, there are  
316 fissure-like (with very large aspects ratio) 2-dimensional pores (2-D pores) which  
317 correspond to the pore group with a mean diameter of 50  $\mu\text{m}$  and 1  $\mu\text{m}$  observed in  
318 Figure 11d. Audiguier et al. (2008) observed similar 2-D pores of a diameter between  
319 0.1 and 1  $\mu\text{m}$  in a natural clay after free swelling.

## 320 **4 INTERPRETATION AND DISCUSSION**

321 After the infiltration test, a decrease of dry density was observed in the lower part ( $h =$   
322 0-40 mm), a dry density close to the initial was obtained in the middle zone ( $h =$   
323 50-150 mm). Several authors (Lemaire et al., 2004; Kröhn, 2003b, 2004; Villar et al.,



324 2008) reported that swelling leads to a displacement of clay particles in the near  
325 wetting end zone, and thus to a significant decrease of dry density. This in turn causes  
326 compaction of the bentonite in the still dry parts. This was obviously not the case in  
327 this study because the resulting compaction in the middle zone was not noticeable: the  
328 value of dry density remained the same after the test. Thereby, the decrease of dry  
329 density in the near wetting end zone may probably due to the soil rebounding due to  
330 the release of swelling pressure. The limited compaction by soil swelling pressure can  
331 be also explained by the fact that the compaction pressure applied for sample  
332 preparation was about 12 MPa, much higher than the soil swelling pressure estimated  
333 at 3 MPa at  $1.67 \text{ Mg/m}^3$  dry density (see Wang et al. 2013). As far as the upper part  
334 (200-250 mm) is concerned, the significant increase of dry density is rather related to  
335 the sample removal. As described previously, the sample was extruded by pushing the  
336 top side with a pressure as high as 12 MPa. This pressure was almost the same as the  
337 pressure applied for the sample compaction. If we consider a yield stress of 12 MPa  
338 for the sample at its initial state, the value must decrease upon hydration. Therefore,  
339 significant compaction can be expected during sample extrusion. However, this  
340 compaction was limited to the upper part because of the contribution of the friction  
341 between the sample and the metallic column. Kröhn (2003b, 2004) performed a  
342 laboratory infiltration test on MX80 bentonite with an initial dry density of  $1.50$   
343  $\text{Mg/m}^3$  and observed similar phenomenon: significant decrease of dry density  
344 occurred in the area near the wetting end (20 mm for a sample of 100 mm long);  
345 no-noticeable changes occurred in the remaining part. In addition, all density changes

346 took place within the first four days, with no time dependence (over 189 days).  
347 Thereby, they considered that the assumption of no migration of bentonite particles in  
348 the specimen is a good approximation except for the first few millimeters (Kröhn,  
349 2004). Therefore, in the test conditions adopted in the present work, it is believed that  
350 the error was very limited when determining the hydraulic conductivity by taking the  
351 mean value of dry density ( $1.67 \text{ Mg/m}^3$ ).

352 From the shape of the suction isochrones shown in Figure 7, it can be observed that  
353 suction changes mainly occurred in the lower part of the sample below 100 mm, and  
354 in the upper part limited changes were identified. This is in agreement with the water  
355 content distribution curve (Figure 5a), where much more change near the wetting end  
356 was observed. As noted by Delage et al. (1998a, b) and Ye et al. (2009), this  
357 phenomenon could be explained by separating the liquid water transfer from the water  
358 vapour diffusion: in the zone near the wetting face, the water transfer involves mainly  
359 the liquid water; by contrast, water vapour diffusion prevails in the zone far from the  
360 wetting face. In fact, infiltration tests performed by Delage et al. (1998a, b) showed  
361 almost vertical suction profiles in all time within the part beyond 50 mm from the  
362 wetting face. As the suction was deduced from the measured relative humidity, they  
363 concluded that at the upper part beyond 50 mm, the water transfer was mainly  
364 governed by vapour diffusion. The less vertical suction profiles in the present work  
365 suggest a relatively less prevailing vapour transfer than that in the case of Delage et al  
366 (1998a, b).

367 By applying Darcy's law, different relationships between hydraulic conductivity and  
368 suction were obtained at different measurement sections (Figure 10). As reported by  
369 Loiseau et al. (2002), Cui et al., (2008) on the Kunigel/sand mixture and Marcial  
370 (2003) on the pure MX80 bentonite, this phenomenon is related to the effect of  
371 hydraulic gradient. In general, when experimentally determining the hydraulic  
372 conductivity based on Darcy's law, a linear relationship between water flow rate ( $q$ )  
373 and hydraulic gradient ( $i$ ) is obtained. However, non-linear relationships are often  
374 observed for clayey soils (Lutz & Kemper, 1959; Miller & Low, 1963; Zou, 1996),  
375 and there is a "critical gradient" below which flow occurs in non-Darcian mode (Yong  
376 and Warkentin, 1975; Dixon et al., 1987). This can be explained by the high energy of  
377 the water adsorbed in clays, which increases with the clay fraction and activity (Dixon  
378 et al., 1987). When the hydraulic gradient increases, this energy is overcome locally  
379 and the adsorbed water can be mobilised. For soils containing highly active clay  
380 minerals such as smectite in this study, this critical gradient effect can be significant  
381 leading to different  $k - s$  relationships obtained at different measurement sections.

382 For clarifying this effect, the water fluxes ( $q$ ) and hydraulic gradient ( $i$ ) for each  
383 suction level (suction from 62 to 32 MPa) are plotted in Figure 13. Bi-linear  
384 relationships can be observed for each suction value, indicating existence of "critical  
385 gradients", their values ranging from 8000 to 38000. To apply Darcy's law, the water  
386 flow was considered only when the linear segment at higher water flux was reached  
387 (details about this method can be found in Dixon et al., 1992).

388 Considering the critical gradient effect (Figure 13), the hydraulic conductivity was  
389 corrected and shown in Figure 14. A unique relationship was obtained between  
390 hydraulic conductivity and suction, independent of the measurement sections. In  
391 Figure 14, the hydraulic conductivity determined by Karnland et al. (2008) for the  
392 same material at the same dry density ( $1.67 \text{ Mg/m}^3$ ) under saturated state is also  
393 presented: a much higher value of  $10^{-13} \text{ m/s}$  was observed. Unlike the non swelling  
394 soils for which the hydraulic conductivity is increasing upon wetting, a “U-shape”  
395 relationship was observed: the hydraulic conductivity decreased when suction  
396 decreased from 65 to about 15 MPa, then increased for further suction decrease.  
397 Similar observations were made on the Kunigel-V1/sand mixture (JNC, 2000; Cui et  
398 al., 2008) and GMZ bentonite (Ye et al., 2009). As explained by Cui et al. (2008) and  
399 Ye et al. (2009), in the beginning water transfer was primarily governed by the  
400 network of large-pores, which were progressively clogged by the expanding hydrated  
401 aggregates, leading to the hydraulic conductivity decrease. When the large-pores  
402 clogging ended and water transfer was controlled by the suction gradient, the common  
403 hydraulic conductivity increase with suction decrease was observed.

404 It was observed in Figure 11a that the intruded mercury void ratio ( $e_{mi}$ ) were lower  
405 than the global soil void ratio ( $e = 0.63$ ). This can be explained by the limited pressure  
406 range of the MIP technique: for the high-plasticity soils, there is a significant pore  
407 volume (entrance diameter smaller than 6 nm) that the mercury could not penetrate to  
408 (Lloret et al., 2003; Delage et al., 2006). Comparison of the curves at different  
409 suctions shows that with decreasing suction (65-38-24.9-12.6 MPa), the amount of

410 intruded porosity decreases. Pusch (1999) and Cui et al. (2002) observed the same  
411 phenomenon and explained by the interaction between large- and small-pores: during  
412 suction decrease under constant-volume conditions the size of non-intruded pores  
413 increased with increasing interlayer space, while the large-pores were filled by small  
414 clay particles.

415 Figure 11b showed that suction decrease did not change the small-pores family,  
416 whereas a decrease of large-pores quantity was observed - it was significant when  
417 suction decreased from 65 MPa to 38 MPa (10%) and much less (3%) for the  
418 subsequent suction decrease (38-24.8-12.6 MPa). This confirms the previous  
419 conclusion that during suction decrease the large-pores were clogged (although at  
420 different rate) by the invasion of exfoliated clay particles whose interlaminar distance  
421 increases upon saturation. This phenomenon could also be identified in the SEM  
422 photograph with high magnification for 38 MPa suction (Figure 12d).

423 For suction lower than 4.2 MPa (Figure 11c), a lower value of  $e_{mi}$  was also obtained  
424 compared to the global void ratio ( $e = 0.63$ ). However, the intruded porosity at these  
425 suctions (4.2, 1 and 0 MPa) was slightly higher than that in the initial state ( $s = 65$   
426 MPa,  $e_{mi} = 0.47$ ). This phenomenon can be attributed to the larger pore quantity of the  
427 pore group having a mean size of 50  $\mu\text{m}$  (for 4.2 and 1 MPa suction) and 1  $\mu\text{m}$  (for  
428 zero suction) compared with the initial state (Figure 11d). These two pores groups  
429 were identified as 2-D pores of about 50 and 1  $\mu\text{m}$  diameter for the saturated sample  
430 in Figure 12e and 12f, respectively. Audiguier et al. (2008) explained the formation of

431 the 2-D pores by the division of clay particles within the aggregates due to swelling.  
432 Moreover, the small deformation induced by the release of swelling pressure before  
433 freeze-drying may also play a role in the large-pores quantity increase. However, this  
434 slight effect could not be identified by the current technique of samples preparation,  
435 and new methods without stress state changes are needed to obtain more accurate  
436 microstructure observations.

437 It appeared that the small-pores changed only when the saturation was approached (1  
438 MPa and 0 MPa in Figure 11 and Figure 12). This phenomenon is in agreement with  
439 the conclusion by Cui et al. (2002) for the Kunigel clay/sand mixture: when water  
440 infiltrated into the soil, the hydration of clay aggregates hydration started first on the  
441 surface giving rise to the clay particles exfoliation and resulting in the clogging of  
442 large-pores, whereas the small-pores remained almost un-affected; the small-pores  
443 started to change only when the water saturation was approached (suction lower than  
444 9 MPa). When saturation was reached, the clay aggregates disappeared (Figure 12f)  
445 and a new pore family of about 1  $\mu\text{m}$  diameter was formed, visible from both MIP and  
446 SEM tests. The small-pores seemed to be compressed by the swelling pressure,  
447 whereas 2-D pores of 1  $\mu\text{m}$  in diameter appeared due to the division of clay particles  
448 within the aggregates (Saiyouri et al., 2000).

449 In order to quantify the suction effect on the large-pores, a large-pores radius larger  
450 than 2  $\mu\text{m}$  was considered based on the curves in Figure 11 where it can be observed  
451 that the proportion of pores larger than 2  $\mu\text{m}$  changed with decreasing suction. Using

452 this limit value that separates large-pores from small-pores, the void ratio  
453 corresponding to the large-pores was derived from the cumulative curves (Figure 11).  
454 The relationship between the calculated large-pore void ratio ( $e_L$ ) and applied suction  
455 are presented in Figure 15. It can be seen that the large-pores quantity was  
456 progressively reduced with decreasing suction in the range of 65 to 12.6 MPa (zone I).  
457 However, the subsequently decrease of suction to 4.2 MPa led to an increase of  
458 large-pores quantity. This can be explained by the creation of the 2-D pores described  
459 above; a significant decrease followed when suction decreased from 1 MPa to zero  
460 (zone II).

461 It is interesting to note that if we relate the large-pore changes (Figure 15) to the  
462 hydraulic conductivity changes (Figure 14), it seems that the hydraulic conductivity  
463 changed following the same trend as the large-pores quantity during hydration. In  
464 other words, water transfer was primarily governed by the network of large-pores in  
465 the full suction range, but not controlled by the suction gradient in the lower suction  
466 range as mentioned above. The large-pores decreased progressively in quantity due to  
467 the clay particles exfoliation occurred on the aggregates surface in the suction range  
468 from 65 to 12.6 MPa, leading to a decrease of hydraulic conductivity. When saturation  
469 was approached (4.2 - 1 MPa), water transfers through the 2-D pores appeared,  
470 leading to an increase in hydraulic conductivity; in saturated state the value can reach  
471 as high as  $10^{-13}$  m/s as reported by Karnland et al. (2008). It should be noted that after  
472 saturation, the hydraulic conductivity has been found to be time dependent (Loiseau et  
473 al., 2002; Cui et al., 2008). It decreased with time due to the re-organization of

474 microstructure over time in the soil sample. After saturation, water in the  
475 inter-aggregate pores is not necessarily in equilibrium with the water inside the  
476 aggregates in terms of water potential. Thus the water re-distribution occurred inside  
477 the soil, leading to a uniform microstructure in long term (Stroes-Gascoyne et al.,  
478 2010).

## 479 **5 CONCLUSION**

480 The hydraulic properties of a compacted bentonite-sand mixture were investigated in  
481 the laboratory by carrying out water retention test and infiltration test as well as the  
482 microstructure observation. The results obtained allowed relating the variation of  
483 hydraulic conductivity to the microstructure changes.

484 During suction decrease (suction higher than 12.6 MPa) the large-pores were clogged  
485 progressively by the exfoliated clay particles (although at different rates); however,  
486 when saturation was approached (suction lower than 4.2 MPa) large-pores quantity  
487 increased again due to the appearance of 2-D pores. The small-pores changed only  
488 when saturation was approached.

489 With suction decrease under constant volume condition, the hydraulic conductivity  
490 decreased followed by an increase after certain suction threshold. This change  
491 followed the same tendency as the large-pores quantity. In other words, water transfer  
492 was primarily governed by the network of large-pores. Over time, the hydraulic  
493 conductivity is expected to decrease due to the water re-distribution among different



494 pore families that leads to a uniform microstructure in long term.

## 495 ACKNOWLEDGEMENTS

496 The work was conducted in the framework of the SEALEX project of IRSN and the  
497 PHC Cai Yuanpei project (24077QE). The support of the National Nature Science  
498 Foundation of China (41030748) and that of the China Scholarship Council (CSC) are  
499 also greatly acknowledged.

## 500 REFERENCES

- 501 AFNOR, 1992. AFNOR NF P94-057, Soils: investigation and testing. Granulometric  
502 analysis. Hydrometer method. Association Francaise de Normalisation. France.
- 503 AFNOR, 1996. AFNOR NF P94-056, Soils: investigation and testing. Granulometric analysis.  
504 Dry sieving method after washing. Association Francaise de Normalisation. France.
- 505 Audiguier, M., Geremew, Z., Cojean, R., 2008. Relations entre les microstructures de deux  
506 sols argileux de la région parisienne et leur sensibilité au retrait gonflement. SEC2008,  
507 Paris, France, 1-3 sept. Editions du LCPC.2008: 235-243.
- 508 Blatz, J.A., Cui, Y. J., Oldecop. L., 2008. Vapour Equilibrium and Osmotic Technique for  
509 Suction Control. *Geotech Geol Eng* (2008) 26:661–673.
- 510 Börgesson, L., Chijimatsu, M., Fujita, T., Nguyen, T.S., Rutqvist, J., Jing, L., 2001.  
511 Thermo-hydro-mechanical characterisation of bentonite-base buffer material by  
512 laboratory tests and numerical back analyses. *International Journal of Rock Mechanics &  
513 Mining Sciences* 38, 95-104.
- 514 Cui, Y. J., Loiseau, C., Delage, P., 2002. Microstructure changes of a confined swelling soil  
515 due to suction controlled hydration Unsaturated soils: proceedings of the Third  
516 International Conference on Unsaturated Soils, UNSAT 2002, 10-13 March 2002, Recife,  
517 Brazil, 593.
- 518 Cui, Y.J., Tang, A..M., Loiseau, C., Delage, P., 2008. Determining the unsaturated hydraulic  
519 conductivity of a compacted sand-bentonite mixture under constant-volume and  
520 free-swell conditions. *Physics and Chemistry of the Earth, Parts A/B/C*, 33(Supplement  
521 1):S462 – S471.
- 522 Daniel, D.E., 1982. Measurement of hydraulic conductivity of unsaturated soils with  
523 thermocouple psychrometers. *Soil Science Society of America Journal* 20  
524 (6):1125–1129.
- 525 Delage, P., Lefebvre, G., 1984. Study of the structure of a sensitive Champlain clay and its  
526 evolution during consolidation. *Canadian Geotechnical Journal* 21 (1), 21–35.

527 Delage P., Howat M., Cui Y.J. 1998a, The relationship between suction and swelling  
528 properties in a heavily compacted unsaturated clay. *Eng Geol* 50(1–2):31–48

529 Delage, P., Cui, Y.J., Yahia-Aissa, M., De Laure, E., 1998b. On the unsaturated hydraulic  
530 conductivity of a dense compacted bentonite. *Proc. of Unsat'98, Beijing, vol. 1*, pp.  
531 344–349.

532 Delage, P., Marcial, D., Cui, Y.J., Ruiz, X., 2006. Ageing effects in a compacted bentonite: a  
533 microstructure approach. *Géotechnique* 56 (5), 291–304.

534 Delage P., Cui Y.J., 2008, An evaluation of the osmotic method of controlling suction,  
535 *Geomechanics and Geoengineering*, 3(1):1-11

536 Dixon, D.A., Cheung, S.C.H., Gray, M.N., Davidson, B.C., 1987. The hydraulic conductivity  
537 of dense clay soils. *Proc. 40th Canadian Geotechnical Conference, Regina, Saskatchewan*  
538 *- Canada*, pp. 389–396.

539 Dixon, D.A., Gray, M.N., Hnatiw, D., 1992. Critical gradients and pressures in dense swelling  
540 clays. *Canadian Geotechnical Journal* 29 (6), 1113–1119.

541 Dixon, D.A., Graham, J., Gray, M.N., 1999. Hydraulic conductivity of clays in confined tests  
542 under low hydraulic gradients. *Canadian Geotechnical Journal* 36 (5), 815- 825.

543 Fredlund, D.G., Rahardjo, H., 1993. *Soil mechanics for unsaturated soils*. John Wiley and  
544 Sons, New York

545 GEISER F. 1999, *Comportement mécanique d'un limon non saturé: étude expérimentale et*  
546 *modélisation constitutive[D]*. Switzerland: Thesis, Ecole Polytechnique Fédérale  
547 de Lausanne, EPFL.

548 HEAD K H. 1980, *Manual of soil laboratory testing, volume 1: soil classification and*  
549 *compaction tests[M]*. London: Pentech Press.

550 JNC, 2000. H12: Project to establish the scientific and technical basis for HLW disposal in  
551 Japan, report TN1410 2000-001, Tokai-Mura.

552 Karnland, O., Nilsson, U., Weber, H., and Wersin, P., 2008. Sealing ability of Wyoming  
553 bentonite pellets foreseen as buffer material-Laboratory results. *Physics and Chemistry*  
554 *of the Earth, Parts A/B/C*, 33:S472–S475.

555 Kenney, T.C., van Veen, W.A., Swallow, M.A., Sungaila, M.A., 1992. Hydraulic conductivity  
556 of compacted bentonite-sand mixtures. *Canadian Geotechnical Journal* 29 (3):  
557 364–374.

558 Komine, H., 2004. Simplified evaluation on hydraulic conductivities of sand-bentonite  
559 mixture backfill. *Applied Clay Science* 26 (1–4), 13–19.

560 Komine, H., 2010. Predicting hydraulic conductivity of sand bentonite mixture backfill before  
561 and after swelling deformation for underground disposal of radioactive wastes.  
562 *Engineering Geology*.

563 Kröhn, K. P., 2003a. New conceptual models for the resaturation of bentonite. *Applied Clay*  
564 *Science* 23 (1-4), 25-33.

565 Kröhn, K. P., 2003b. Results and interpretation of bentonite resaturation experiments with  
566 liquid water and water vapour. In: Schanz, T. (Ed.), *Proceedings of the International*  
567 *Conference from Experimental Evidence towards Numerical Modeling of Unsaturated*  
568 *Soils, Weimar, Germany, vol. 1*. Springer, Berlin, pp. 257–272.

569 Krohn, K, 2004, *Report GRS-199, Modelling the Re-Saturation of Bentonite in Final*  
570 *Repositories in Crystalline Rock*, ISBN 3-931995-66-6

571 Lemaire, T., Moyne, C., Stemmelen, D., 2004. Imbibition test in a clay powder (MX-80  
572 bentonite. *Applied Clay Science* 26: 235-248.

573 Lloret, A., Villar, M.V., Sanchez, M., Gens, A., 2003. Mechanical behaviour of heavily  
574 compacted bentonite under high suction changes. *Géotechnique*, 53(1):27–40.

575 Loiseau, C., Cui, Y.J., Delage, P., 2002. The gradient effect on the water flow through a  
576 compacted swelling soil. *Proc. 3rd Int Conf Unsaturated Soils, UNSAT'2002 Recife,*  
577 *Brazil, Balkema*, vol. 1, pp. 395-400.

578 Lutz, J.F., Kemper, W.D., 1959. Intrinsic permeability of clay as affected by clay-water  
579 interaction. *Soil science* 88: 83-90.

580 Marcial, D., 2003. Comportement hydromécanique et microstructural des matériaux de  
581 barrière ouvrageée. Ph.D. thesis, École nationale des ponts et chaussées, Paris, France

582 Miller, R.J., Low, P.F., 1963. Threshold Gradient for Water Flow in Clay Systems. *Soil*  
583 *Science Society of America Journal*. 27 (6):605-609.

584 Pusch, R., 1979. Highly compacted sodium bentonite for isolating rock-deposited radioactive  
585 waste products. *Nucl. Technol. (United States)*, 45(2).

586 Pusch, R., 1999. Microstructural evolution of buffers. *Engineering geology*. 54:33-41.

587 Pusch, R., Yong, R., 2003. Water saturation and retention of hydrophilic clay  
588 buffer-microstructural aspects. *Applied Clay Science*, 23:61-68.

589 Saiyouri, N., Hicher, P.Y., Tessier, D., 2000. Microstructural approach and transfer water  
590 modeling in highly compacted unsaturated swelling clays. *Mechanics of*  
591 *Cohesivefrictional Materials* 5, 41–60.

592 Stepkowska, E.T.: Aspects of the clay electrolyte water-system with special reference to the  
593 geotechnical properties of clays. *Eng. Geol.* 28(3-4), 249–267 (1990)

594 Stroes-Gascoyne, S., 2010. Microbial occurrence in bentonite-based buffer, backfill and  
595 sealing materials from large-scale experiments at AECL's underground research  
596 laboratory. *Applied Clay Science*, 47(1-2):36–42.

597 Tang, A. M. & Cui, Y. J., 2005. Controlling suction by the vapour equilibrium technique at  
598 different temperatures and its application in determining the water retention properties of  
599 MX80 clay. *Can. Geotech. J.* 42 (1): 287-296.

600 Tang, C.S., Tang, A.M., Cui, Y.J., Delage, P., Barnichon, J.D., Shi, B., 2011. A study of the  
601 hydro-mechanical behaviour of compacted crushed argillite. *Engineering Geology*. 118  
602 (3-4):93-103.

603 Thomas, H.R., Cleall, P.J., Chandler, N., Dixon, D., Mitchell, H.P., 2003. Water infiltration  
604 into a large-scale in-situ experiment in an underground research laboratory.  
605 *Geotechnique* 53, 207-224.

606 Van Genuchten, M.T., 1980. A closed-form equation for predicting the hydraulic conductivity  
607 of unsaturated soils. *Soil Science Society of America Journal*, 44: 892-898.

608 Villar, M.V.; Romero, E. & Lloret, A. 2005. Thermo-mechanical and geochemical effects on  
609 the permeability of high-density clays. In: Alonso, E.E. & Ledesma, A.(eds.) *Advances*  
610 *in understanding engineered clay barriers*. A.A. Balkema Publishers, Leiden: 177-191.

611 Villar, M.V., Lloret, A., 2008. Influence of dry density and water content on the swelling of a  
612 compacted bentonite. *Applied Clay Science*, 39(1-2):38-49.

613 Villar, M.V., Gómez-Espina, R. Campos, R., Barrios, I. & Gutiérrez-Nebot, L. 2012. Porosity  
614 Changes Due To Hydration Of Compacted Bentonite. In: Mancuso, C.; Jommi, C. &

615 D'Onza, F. (Eds.): Unsaturated Soils: Research and Applications, Volume 1, pp. 137-144.  
616 Springer, Berlin.

617 Wang, Q., Tang, A. M., Cui, Y. J., Delage, P., Gatmiri. B., 2012. Experimental study on the  
618 swelling behaviour of bentonite/claystone mixture. *Engineering Geology*. 124:59-66.

619 Wang, Q., Tang, A.M., Cui, Y.J., Barnichon, J.D. Delagen P., Ye, W.M., 2013. Voids effects on the  
620 hydro-mechanical behaviour of compacted bentonite-sand mixture. *Soils and Foundations*  
621 53(2), 232-245.

622 Ye, W.M., Cui, Y.J., Qian, L.X., Chen. B., 2009. An experimental study of the water transfer  
623 thro ugh confined compacted GMZ bentonite. *Engineering Geology*, 108(3-4):169–176.

624 Yong, R.N., Warkentin, B.P., 1975. Soil properties and behaviour. Elsevier, Amsterdam.

625 Yong, R.N., Boonsinsuk, P., and Wong, G., 1986. Formulation of backfill material for a  
626 nuclear fuel waste disposal vault. *Canadian Geotechnical Journal*, 23(2):216-228.

627 Zou, Y., 1996. A non-linear permeability relation depending on the activation energy of pore  
628 liquid. *Géotechnique* 46 (4), 769-774.

629

630

631

632 **List of Tables**

633

634 Table 1. Chemical composition of the synthetic water

635 Table 2. Tests performed for water retention property and microstructure observation

636

637

638 **List of Figures**

639

640 Figure 1. Grain size distribution of the MX80 bentonite and sand

641 Figure 2. Schematic setup of the infiltration cell

642 Figure 3. Constant volume cell for WRC determination; (a) osmotic method; (b) vapour  
643 equilibrium technique

644 Figure 4. WRCs of bentonite/sand mixture under constant-volume conditions

645 Figure 5 Water content and dry density distributions after dismantling of the sample

646 Figure 6. Evolution of relative humidity during water infiltration

647 Figure 7. Suction profiles at different times

648 Figure 8. Determination of hydraulic gradient and water flux: (a) hydraulic gradient; (b) rate of  
649 water flow

650 Figure 9. Calculated and measured water volume into the sample

651 Figure 10. Hydraulic conductivity versus suction for different measurement sections

652 Figure 11. Pore size distributions of the bentonite-sand mixture wetted with different suctions  
653 under constant volume conditions

654 Figure 12. SEM photographs of bentonite/sand mixture samples equilibrated at different  
655 suctions

656 Figure 13. Water flux versus hydraulic gradient for different suctions

657 Figure 14. Hydraulic conductivity versus suction

658 Figure 15. Changes of large-pore void ratio with suction

659

660

661

662

663

664

665

666

667 Table 1. Chemical composition of the synthetic water

Components	NaHCO <sub>3</sub>	Na <sub>2</sub> SO <sub>4</sub>	NaCl	KCl	CaCl <sub>2</sub> .2H <sub>2</sub> O	MgCl <sub>2</sub> .6H <sub>2</sub> O	SrCl <sub>2</sub> .6H <sub>2</sub> O
Mass (g) per litre of solution	0.28	2.216	0.615	0.075	1.082	1.356	0.053

668

669 Table 2. Tests performed for water retention property and microstructure observation

Suction (MPa)	Suction control method and duration	Microstructure	
		MIP	SEM
38	Vapour (2 months)	√	√
24.9		√	
12.6		√	
9.0			
4.2		√	√
1	Osmotic (2 months)	√	
0.1			
0	Distilled water (2 months)	√	√
65	Initial suction	√	√

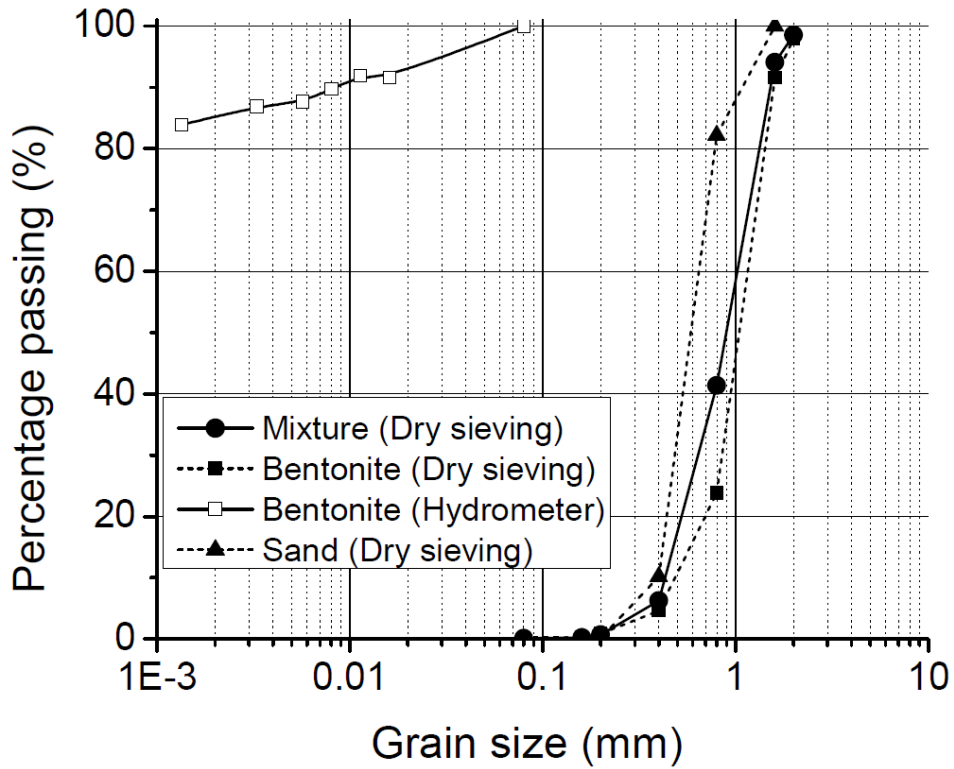
670

671

672

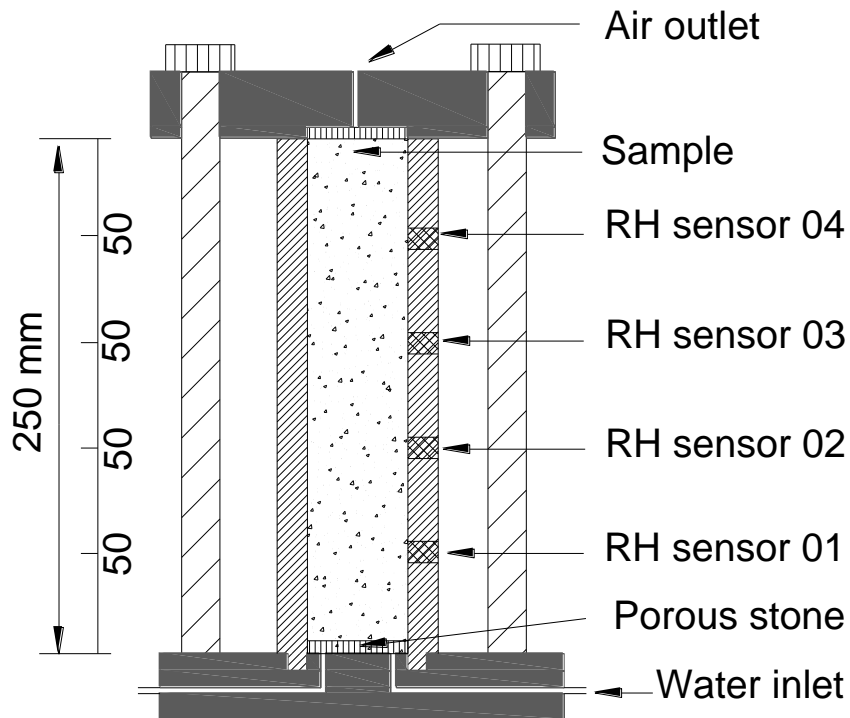
673

674



675

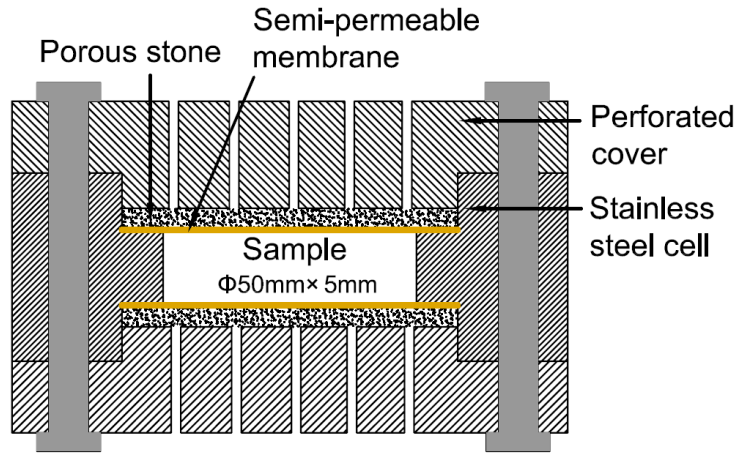
676 Figure 1. Grain size distribution of the MX80 bentonite and sand



677

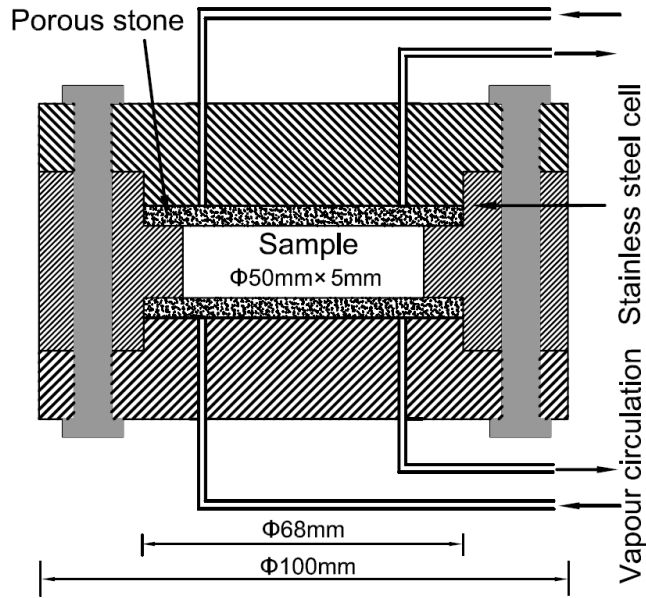
678

Figure 2. Schematic setup of the infiltration cell



679  
680

(a)

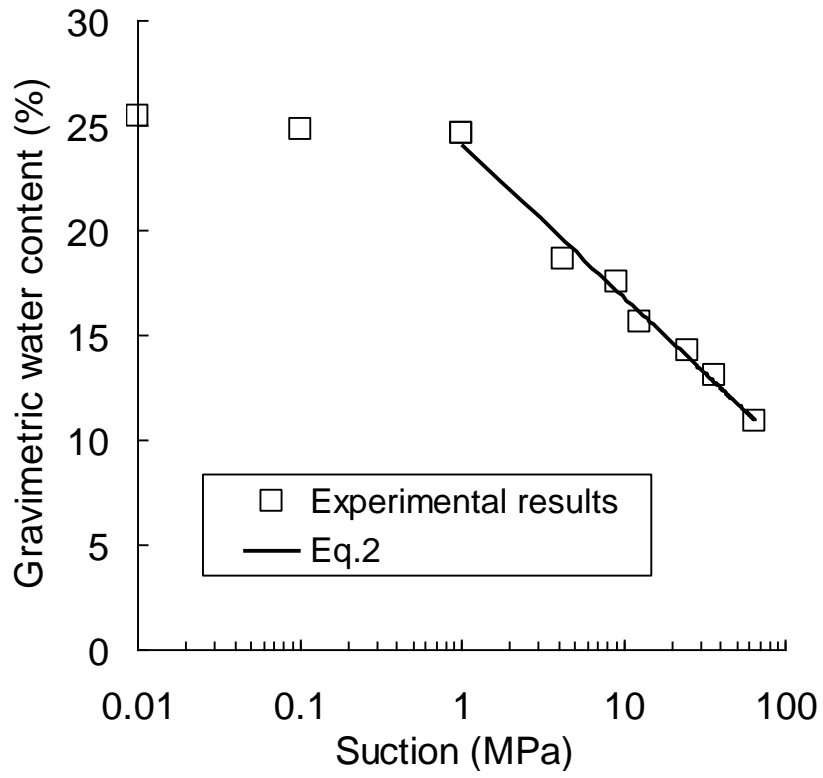


681  
682

(b)

683 Figure 3. Constant volume cell for WRC determination; (a) osmotic method (controlling of  
684 matric suction); (b) vapour equilibrium technique (controlling of total suction)

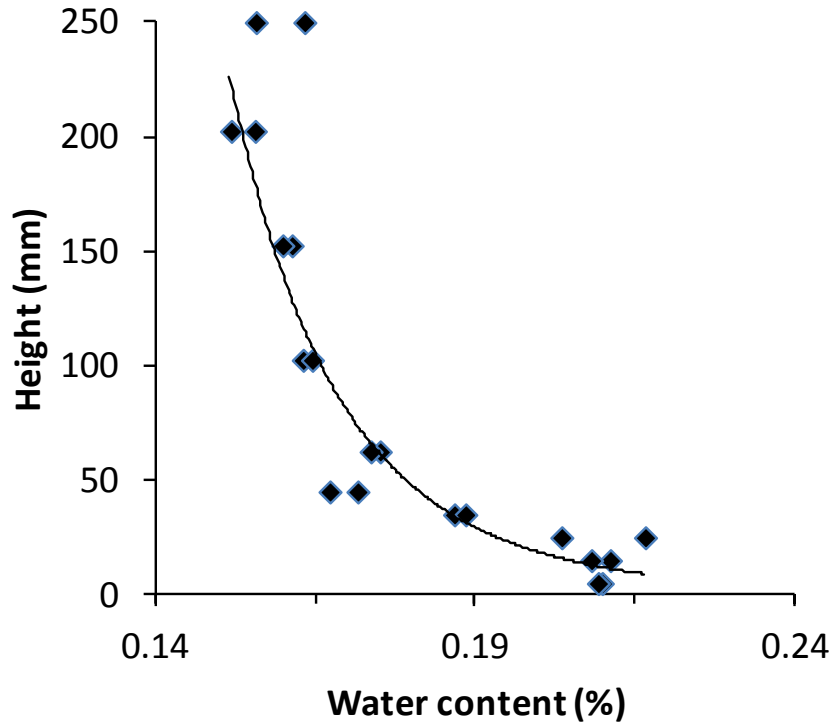




685

686 Figure 4. WRC of bentonite/sand mixture under constant-volume conditions

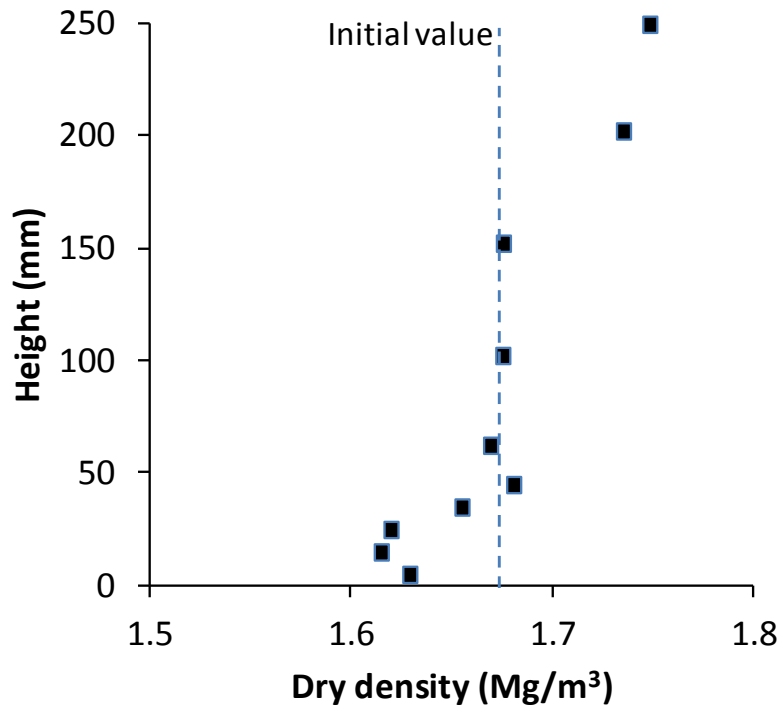
687



688

689

(a) water content distribution



690

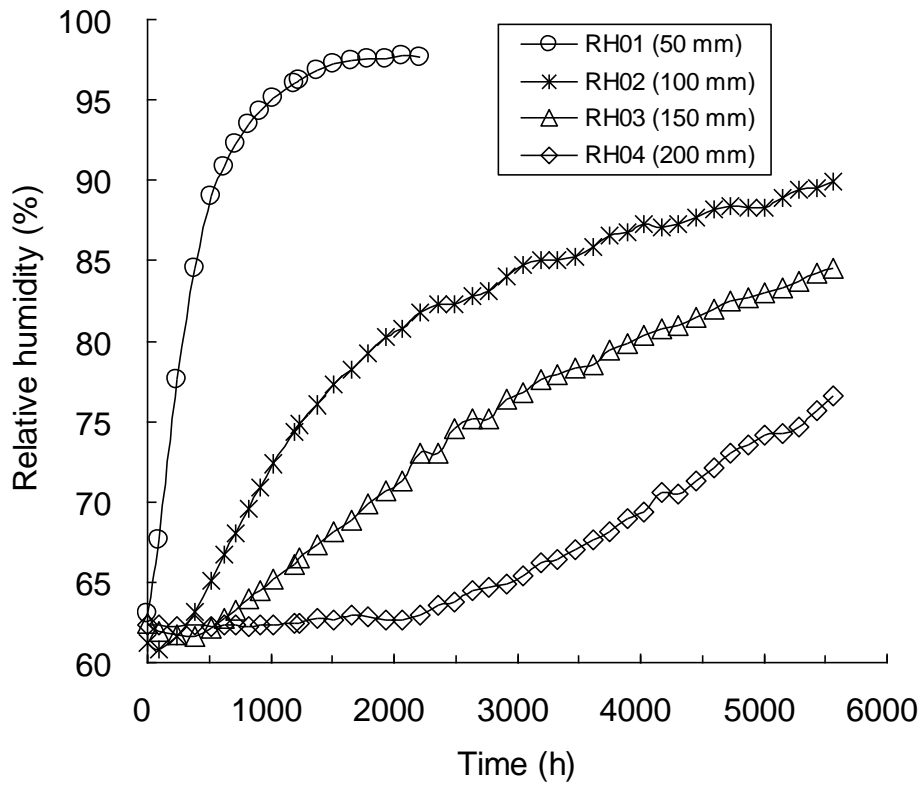
691

(b) dry density distribution

692

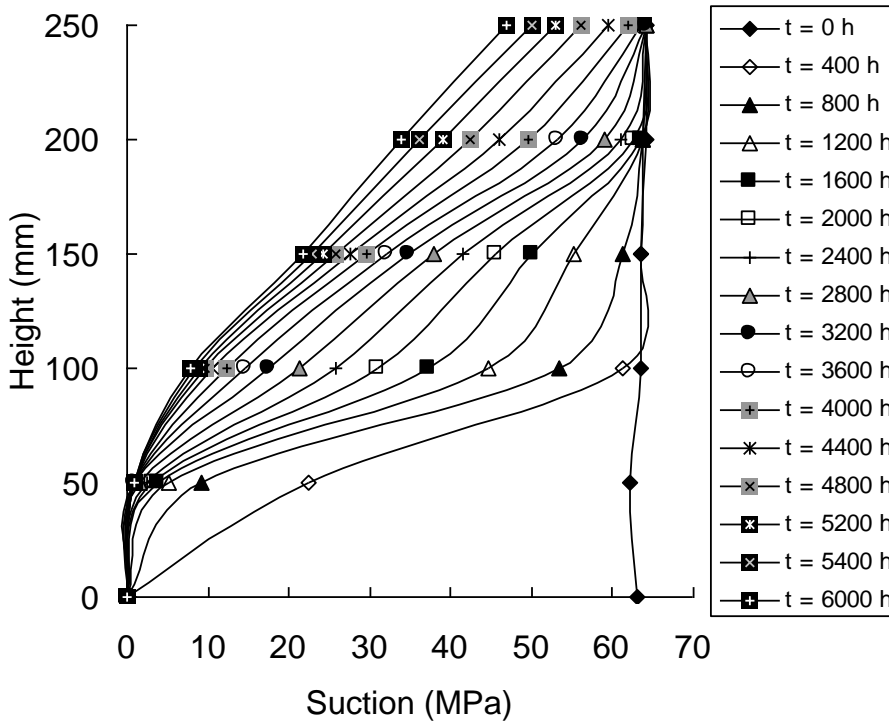
Figure 5 Water content and dry density distributions after dismantling of the sample

693



694

695 Figure 6. Evolution of relative humidity during water infiltration

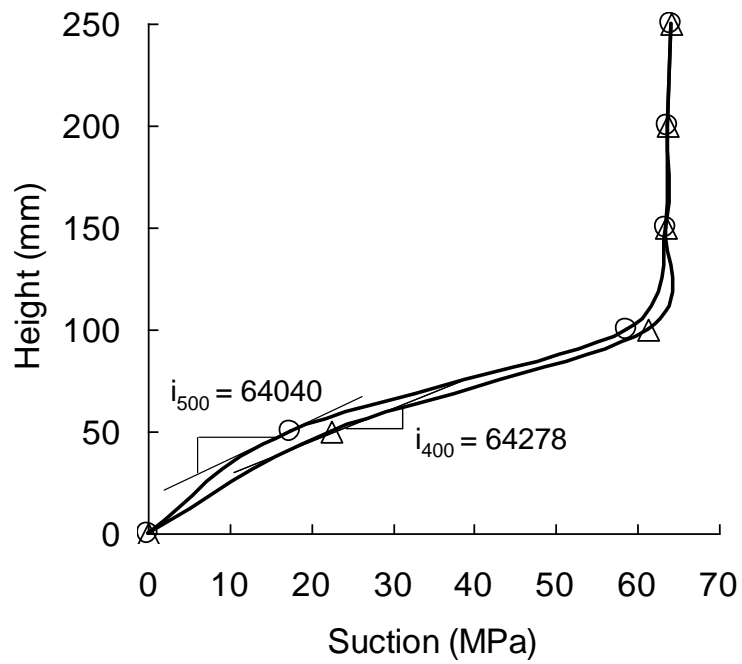


696

697 Figure 7. Suction profiles at different times (Note: There were no measurements at height 250 mm.

698 The values plotted in the figure were extrapolated from the measurements at lower heights)

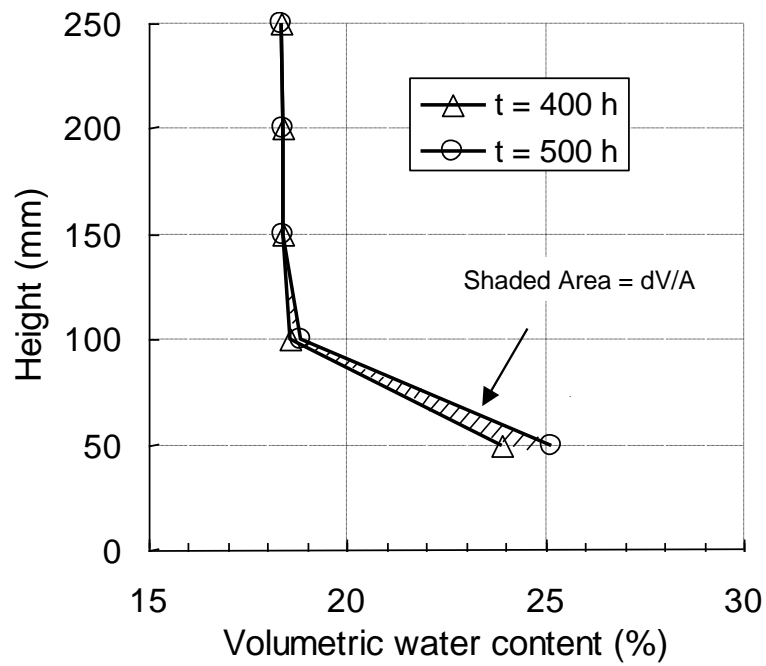
699



700

701

(a)



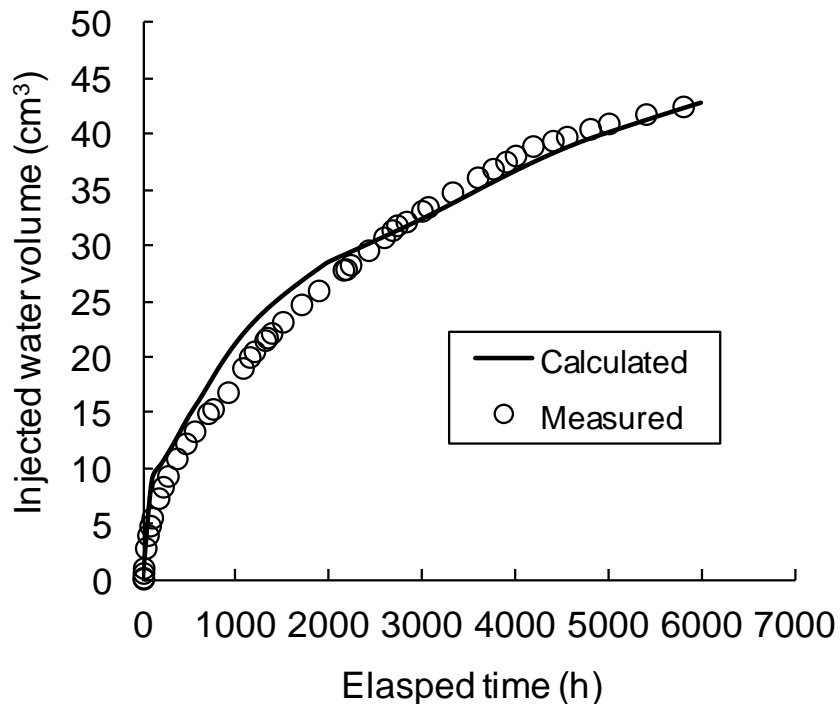
702

703

(b)

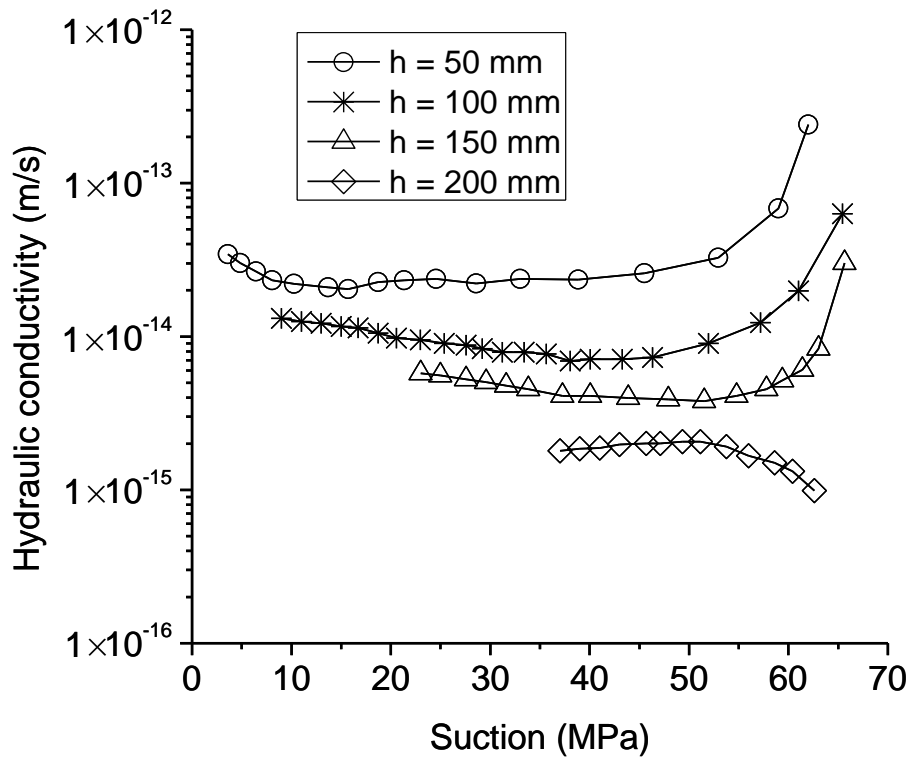
704 Figure 8. Determination of hydraulic gradient and water flux for two times (400 and 500 h)  
 705 during infiltration: (a) hydraulic gradient; (b) rate of water flow

706



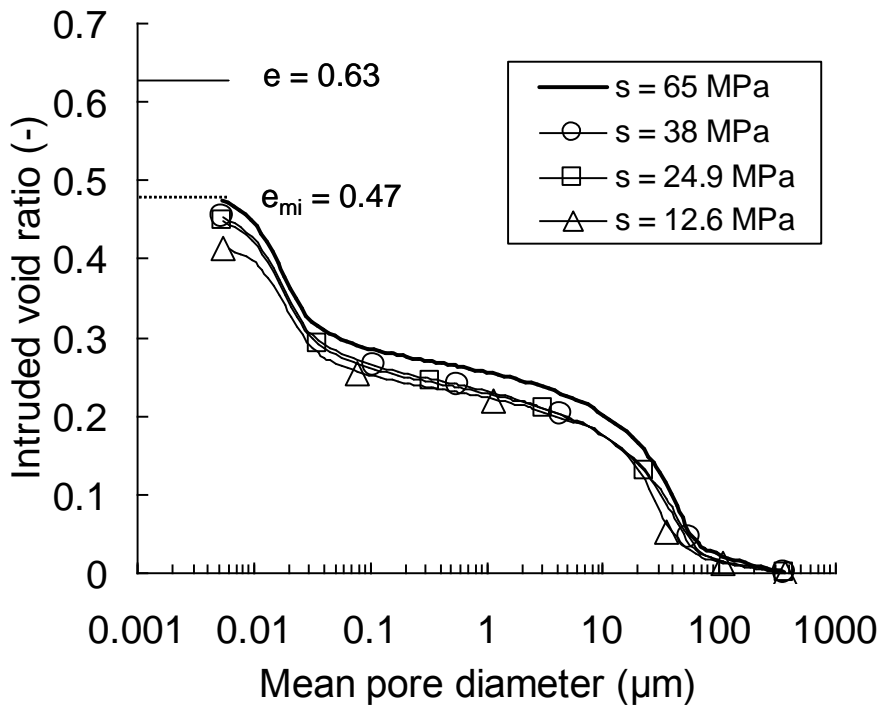
707

708 Figure 9. Calculated and measured water volume into the sample



709

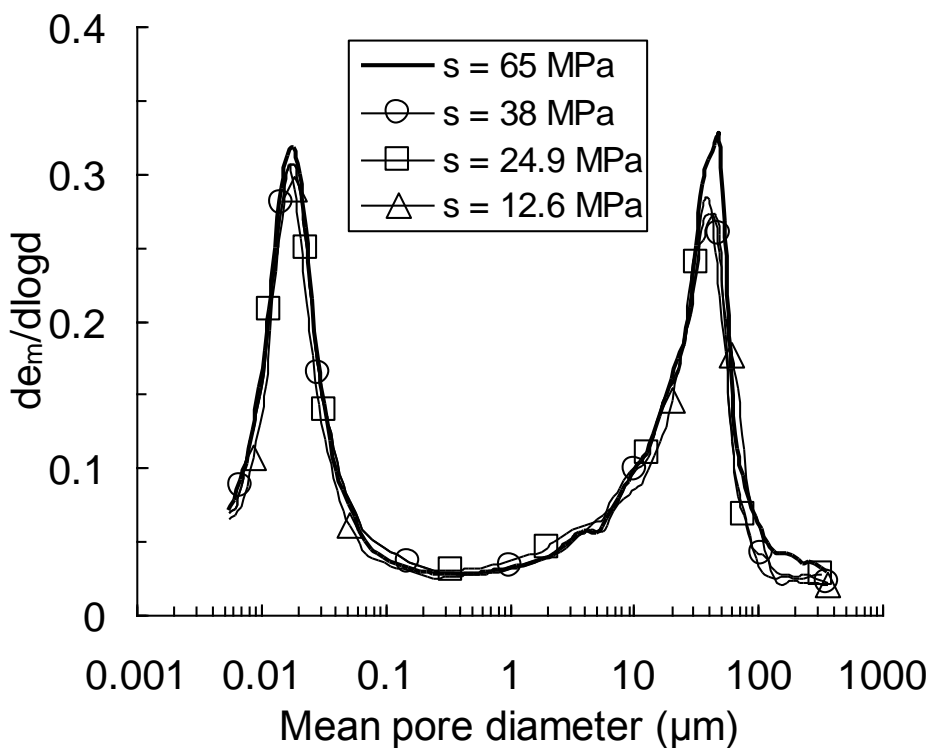
710 Figure 10. Hydraulic conductivity versus suction for different measurement sections (“h”  
 711 represents the distance from hydration surface



712

713

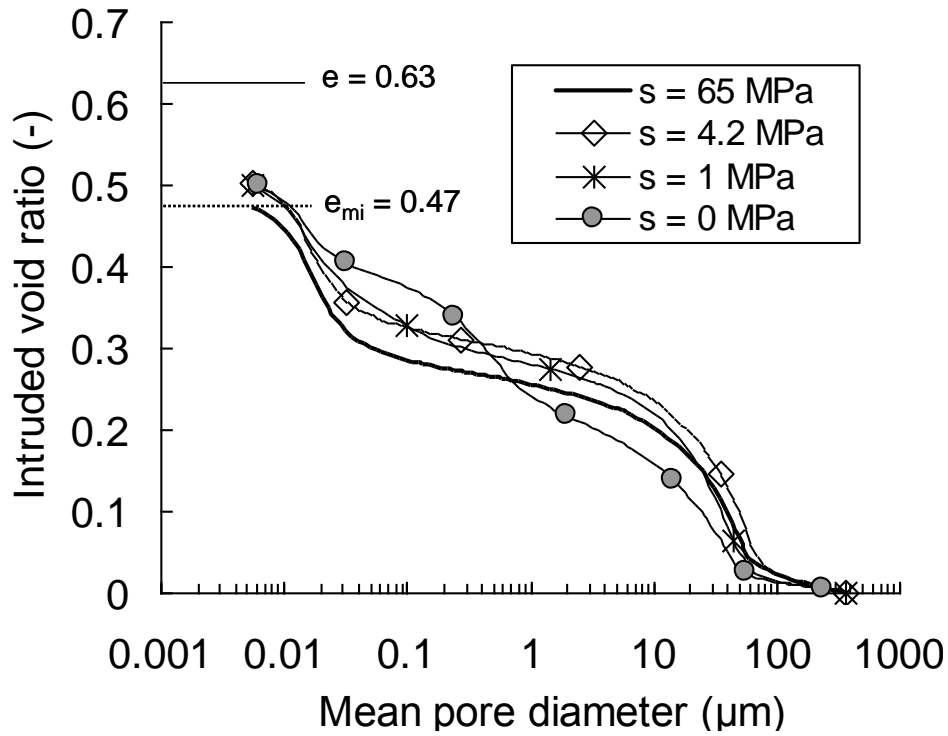
(a) 65 - 12.6 MPa suction



714

715

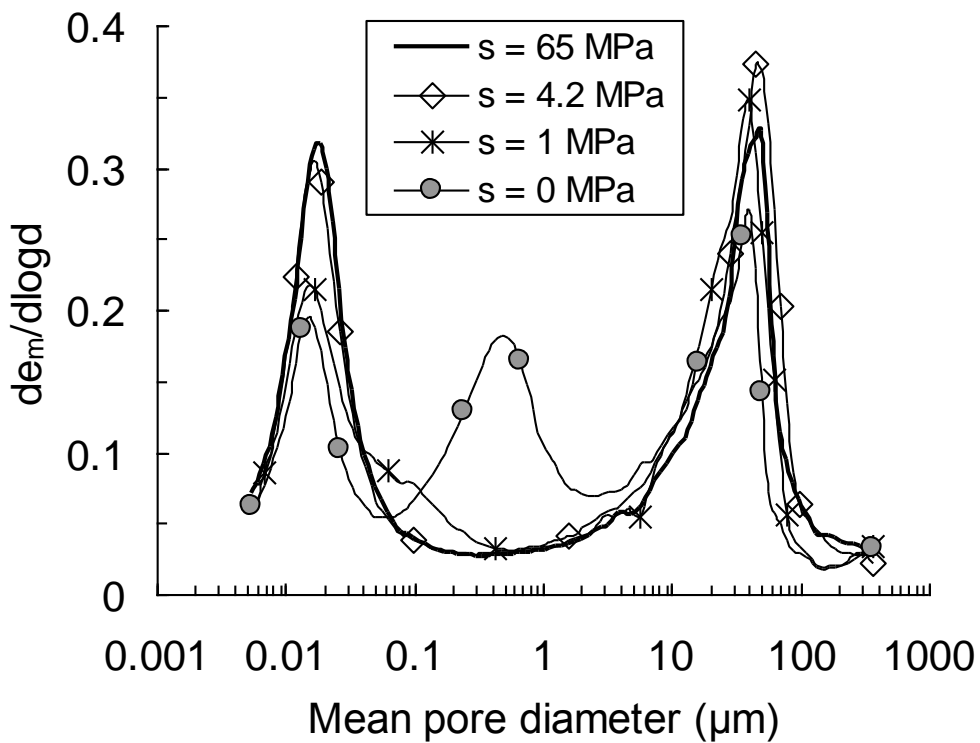
(b) 65 - 12.6 MPa suction



716

717

(c) 4.2 – 0 MPa suction



718

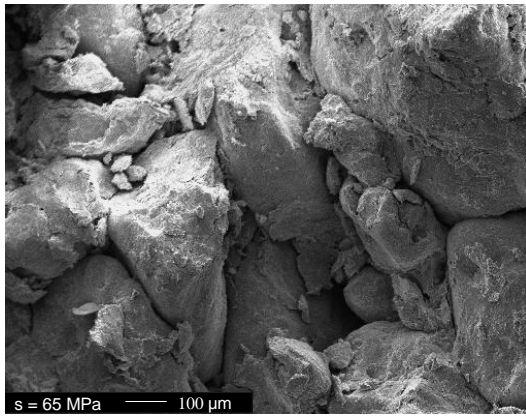
719

(d) 4.2 – 0 MPa suction

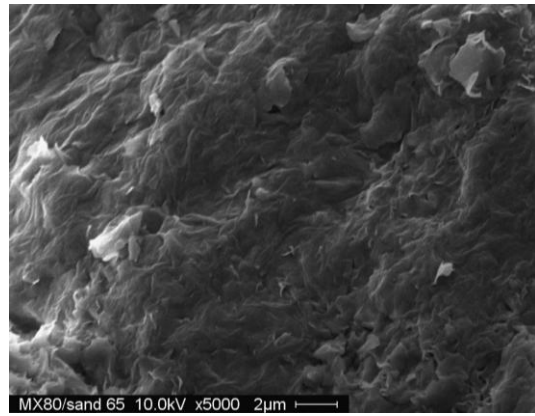
720 Note: symbols plotted in the figure do not correspond to all the measurement points, just a few  
 721 symbols in each curve are plotted for distinction.

722 Figure 11. Pore size distributions of the bentonite-sand mixture wetted with different suctions

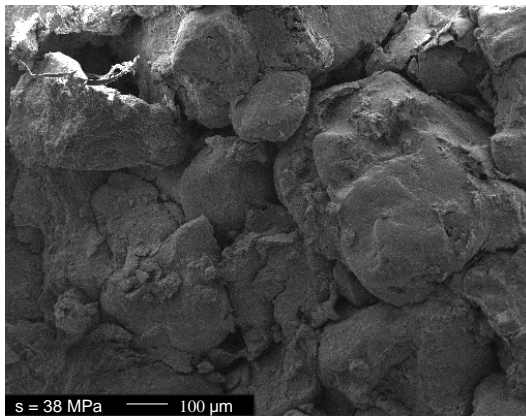
723 under constant volume conditions



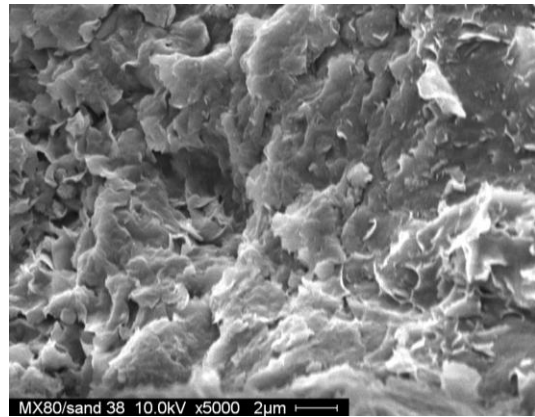
(a)  $s = 65$  MPa (1250 x 1000  $\mu\text{m}$ )



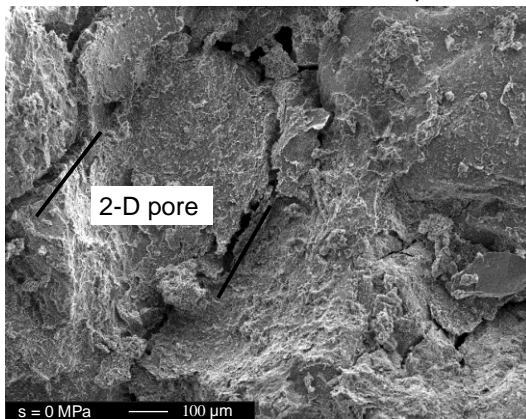
(b)  $s = 65$  MPa (25 x 20  $\mu\text{m}$ )



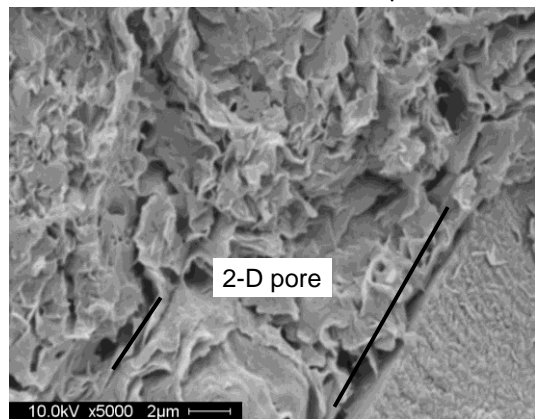
(c)  $s = 38$  MPa (1250 x 1000  $\mu\text{m}$ )



(d)  $s = 38$  MPa (25 x 20  $\mu\text{m}$ )



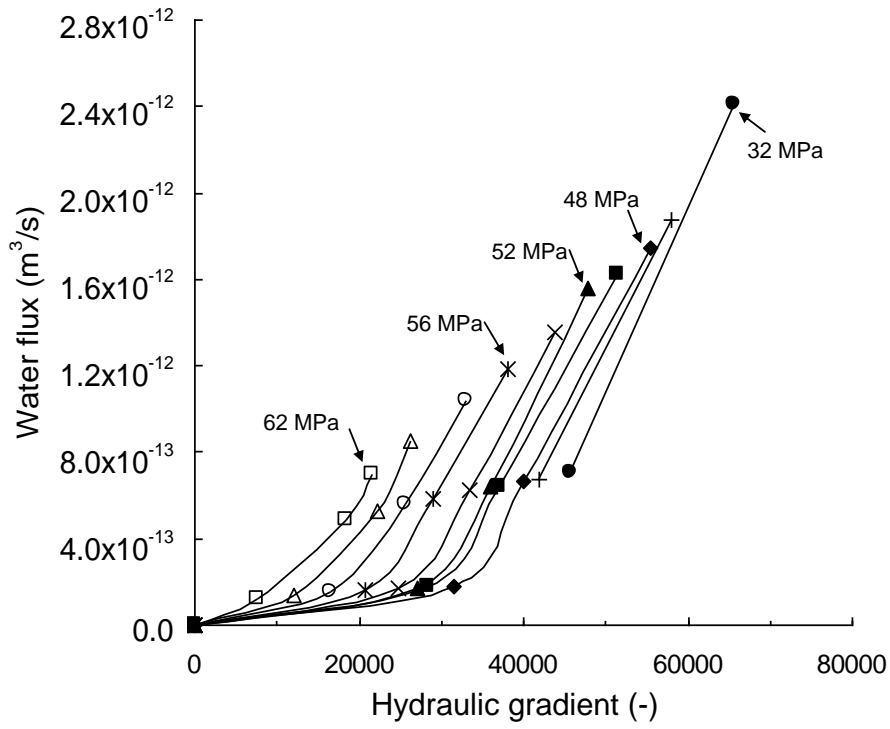
(e)  $s = 0$  MPa (1250 x 1000  $\mu\text{m}$ )



(f)  $s = 0$  MPa (25 x 20  $\mu\text{m}$ )

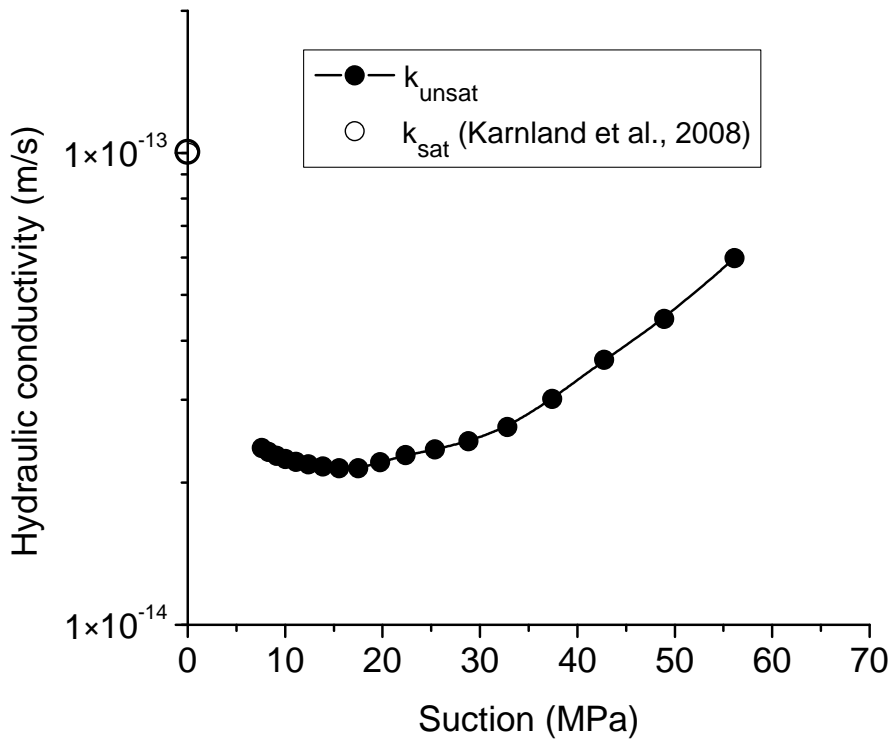
724 Figure 12. SEM photographs of bentonite/sand mixture samples equilibrated at different  
725 suctions





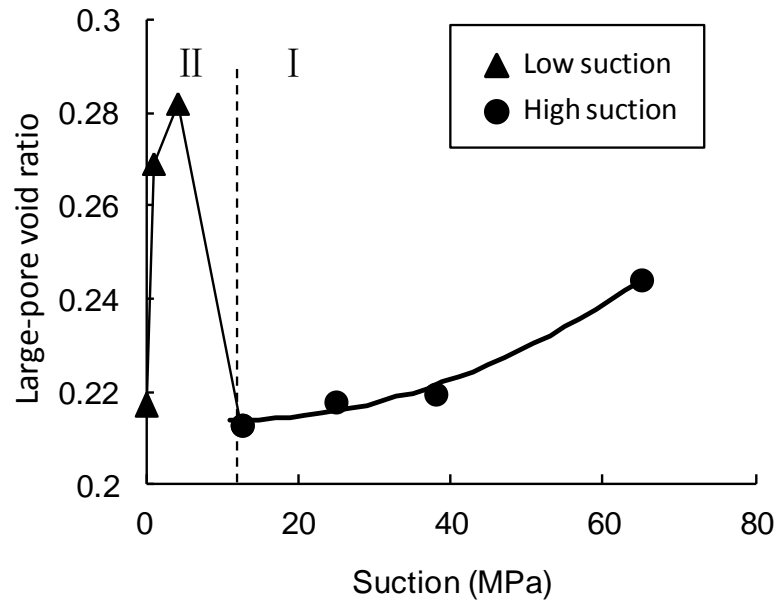
726

727 Figure 13. Water flux versus hydraulic gradient for different suctions



728

729 Figure 14. Hydraulic conductivity versus suction



730

731 Figure 15. Changes of large-pores void ratio (diameter larger than 2  $\mu\text{m}$ ) with suction